JOURNAL OF AIRCRAFT
Vol. 47, No. 1, January–February 2010

Prediction of Tiltrotor Vibratory Loads with Inclusion of Wing–Proprotor Aerodynamic Interaction

Massimo Gennaretti,* Marco Molica Colella,† and Giovanni Bernardini‡
Roma Tre University, 00146 Rome, Italy

DOI: 10.2514/1.41825

A numerical methodology for the prediction of vibratory loads arising in wing–proprotor systems is presented. It is applicable to tiltrotor operating conditions ranging from airplane to helicopter-mode flights. The aeroelastic formulation applied takes into account the aerodynamic interaction effects dominated by the impact between proprotor wake and wing, along with the mutual mechanical influence between elastic wing and proprotor blades. A boundary integral formulation suited for configurations where strong body–vortex interactions occur yields the aerodynamic loads, and beamlike models are used to describe the structural dynamics. A harmonic balance approach is applied to determine the aeroelastic solution. In the numerical investigation, first, the aerodynamic solver is validated by correlation with experimental and numerical results available in the literature, then the vibratory loads transmitted by the wing–proprotor system to the airframe are predicted, focusing the attention on the analysis of the different aerodynamic contributions.

Nomenclature

$\mathbf{f}_{\text{aer}}$	=	vector of generalized aerodynamic forces
$\mathbf{f}_{\text{str}}^{\text{nl}}$	=	vector of nonlinear structural contributions
G	=	Green function
K_b, K_w	=	radius of gyration of blade and wing cross sections
L_v^b, L_w^b, M_ϕ^b	=	blade sectional aerodynamic loads
L_v^w, L_w^w, M_ϕ^w	=	wing sectional aerodynamic loads
$\mathbf{M}$, $\mathbf{C}$, $\mathbf{K}$	=	mass, damping, and stiffness matrices
M_x, M_y, M_z	=	wing moments from pylon and proprotor
m_0^b, m_0^w	=	blade and wing reference masses per unit length
p_x, p_y, p_z	=	blade section inertial forces
$\mathbf{q}$	=	vector of generalized coordinates
q_x, q_y, q_z	=	blade section inertial moments
S_B^p, S_W^p	=	proprotor body and wake surfaces
S_B^w, S_W^w	=	wing body and wake surfaces
T	=	blade tension
t	=	time
$\mathbf{u}_I$	=	velocity induced by far wake
V_x, V_y, V_z	=	wing forces from pylon and proprotor
$\mathbf{v}$	=	body velocity
v_b, w_b	=	displacements of blade elastic axis
v_w, w_w	=	displacements of wing elastic axis
x	=	blade and wing spanwise coordinate
$\mathbf{x}$, $\mathbf{y}$	=	observer and source position
$\mathbf{x}_b$, $\mathbf{x}_w$	=	blade and wing section degrees of freedom
β_c, β_s	=	gimbal degrees of freedom
θ_b, θ_w	=	blade and wing section pitch angle
ϑ	=	time delay
κ_b, κ_w	=	blade and wing torsion rigidity
Λ_1^b, Λ_2^b	=	flap and lead-lag blade bending stiffnesses
Λ_1^w, Λ_2^w	=	flap and chordwise wing bending stiffnesses
μ_w	=	wing mass radius of gyration
ϕ_b, ϕ_w	=	blade and wing elastic torsion deflection
φ	=	velocity potential
χ	=	normal velocity on the body
$\dot{}$	=	time derivative
$'$	=	space derivative

Received 27 October 2008; revision received 2 August 2009; accepted for publication 13 September 2009.

*Associate Professor, Mechanical and Industrial Engineering Department, Via della Vasca Navale 79; m.gennaretti@uniroma3.it.

†Ph.D. Student, Mechanical and Industrial Engineering Department, Via della Vasca Navale 79.

‡Research Engineer, Mechanical and Industrial Engineering Department, Via della Vasca Navale 79.

I. Introduction

THIS paper presents a numerical methodology for the aeroelastic analysis of tiltrotor configurations. In particular, it is aimed at the prediction of the vibratory loads transmitted to the airframe, which are due to the hub loads generated by the proprotor, along with the aerodynamic interactions between wing and proprotor.

In the past 30 years, much of the rotorcraft community effort has been aimed at the design of reliable vertical takeoff and landing vehicles both for civil and military use. Among the different solutions, the tiltrotors have shown to be an optimal combination between helicopter maneuverability and airplane high-flight speed. In the development of tiltrotor technology, stability and comfort enhancement is an important issue that requires the availability of computational tools yielding accurate aeroelastic predictions. Indeed, the development of reliable tools for design of tiltrotors is one of the fields where the rotorcraft community has been focusing much of its research activity. In the pioneering work of Johnson (see, for instance, [1–3]), the emphasis was on the development of a few degree-of-freedom structural modeling of tilting proprotors supported by cantilever wings. Later work, based upon multibody and finite element approaches applied to tiltrotor configurations has provided more accurate description of the wing–proprotor structural dynamics (see, for instance, [4–6]).

It should be noted, however, that most of the tiltrotor aeroelastic models developed in the past have been based on the application of the aerodynamic loads given by quasi-steady strip theories, thereby ignoring or including with rough approximation the aerodynamic interaction effects occurring between wing and proprotors. This may lead to an underestimation of the vibratory loads acting on the airframe and, correspondingly, of the effect they may have on the fatigue life of the structures and on cabin comfort quality. Indeed, wing–proprotor aerodynamic interference is a source of vibratory loads because the proprotor-wake–wing interaction produces significant pressure perturbations, which excite the wing at the blade passage frequency and, in addition, contributes to the azimuthal asymmetry of aerodynamic loads on proprotor blades. Therefore, coupling the structural model with an accurate tool for the solution of the aerodynamic field is essential for tiltrotor design, where prediction and reduction of the vibratory level are of great interest [7].

To this aim the aerodynamic model applied has to be able to analyze three-dimensional unsteady flows and to predict the shape of the wakes and the wing–proprotor interaction effects.

In the past, several works have analyzed the aerodynamic interference between propellers and wings, both from theoretical/numerical and experimental points of view. For instance, [8] presents the results from a panel method code concerning the investigation of the effect of the V-22 airframe on the proprotor loads. Also, in [9], the propeller–wing interaction has been examined numerically using an inviscid, quasi-steady approximation. Moreover, in [10], wing aerodynamic loads under propeller influence have been analyzed, and in [11–13], numerical simulations have been correlated with experimental wind-tunnel data concerning a wing–propeller system. Additional review of the research work concerning propeller–wing aerodynamics is given in [14].

In the present paper, the aerodynamic model applied for the evaluation of the vibratory loads is based on a boundary integral formulation for the velocity potential that is able to capture the effects of the aerodynamic interference between wing and proprotor [15]. In the past, this approach has been successfully applied to the aerodynamic/aeroelastic/aeroacoustic analysis of helicopter configurations with strong blade/wake interactions [16]. This formulation is fully three-dimensional, can be applied to complete aircraft/rotorcraft configurations in arbitrary motion, and allows the calculation of both wake distortion (free-wake analysis) and pressure field forcing the structure. The structural dynamics of wing and proprotor blades is described by beamlike models, with inclusion of the wing–proprotor mechanical interaction, that is mainly governed by the influence of wing deformation on proprotor blades kinematics and by transmission of proprotor loads to the wing through hub and pylon. This formulation yields a set of coupled, nonlinear, integro-differential equations, governing bending and torsion of wing and proprotor blades. Additional equations are included when a gimballed proprotor is examined. Then, the resulting wing/pylon/proprotor aeroelastic model is solved through the application of the Galerkin method for space discretization, followed by a harmonic balance approach for time integration [17].

The objective of the numerical investigation consists of two phases: first, considering a wing–proprotor system in airplane configuration, the boundary integral equation aerodynamic formulation is validated by comparison with experimental and numerical data available in the literature, then the aeroelastic solver is applied to predict the vibratory loads arising on a wing–proprotor system in airplane-mode and helicopter-mode conditions, focusing the attention on the analysis of the importance of the different aerodynamic contributions.

II. Wing–Proprotor Aerodynamic Model

The aerodynamics of wing–proprotor systems is significantly affected by the interactions occurring between proprotor blades and wing. The periodic blade passages close to the wing are an important source of oscillations in wing and blade pressure fields, but in several flight configurations the unsteady aerodynamic loads over the wing are dominated by the impact between wing and vortices of proprotor wake. For instance, this occurs in airplane-mode configurations where the wake vorticity released by the blades massively impinges on the wing portion located behind the propeller, thus generating local flow and pressure perturbations that, in turn, contribute to the vibratory loads transmitted to the airframe. The analysis of aerodynamic problems involving the strong interaction between vortices and bodies is a complex task that requires the application of a suited solver. In this work, the unsteady wing–proprotor aerodynamics are analyzed through the boundary integral formulation for potential flows introduced in [15] as a development of the formulation presented in [18] and further extended to rotors in forward flight in [19].

For the unsteady incompressible flow around a wing–proprotor system the velocity potential field φ may be described through the following boundary integral representation [18,19]:

$$\varphi(\mathbf{x},t)=\int_{S_B^w\cup S_B^p}\left(G\frac{\partial\varphi}{\partial n}-\varphi\frac{\partial G}{\partial n}\right)\mathrm{d}S(\mathbf{y})-\int_{S_W^w\cup S_W^p}\Delta\varphi\frac{\partial G}{\partial n}\,\mathrm{d}S(\mathbf{y}) \quad (1)$$

where S_B^w, S_B^p and S_W^w, S_W^p denote wing and proprotor body and wake surfaces, respectively, and $G=-1/4\pi r$ is the unit-source solution of the 3-D Laplace equation, with $r=\|\mathbf{y}-\mathbf{x}\|$. The impermeability boundary condition on S_B^w and S_B^p yields $\partial\varphi/\partial n=\mathbf{v}\cdot\mathbf{n}$, with $\mathbf{v}$ representing the body velocity and $\mathbf{n}$ its outward unit normal. In addition, $\Delta\varphi$ is the potential jump across the wake surfaces, that is known from the past history of the potential discontinuity at the trailing edge of the corresponding body through the Kutta–Joukowski condition; that is

$$\Delta\varphi(\mathbf{x}_W,t)=\Delta\varphi(\mathbf{x}_W^{\mathrm{TE}},t-\vartheta)$$

with $t-\vartheta$ denoting the instant when the wake material point currently in $\mathbf{x}_W$ emanated from the trailing-edge point $\mathbf{x}_W^{\mathrm{TE}}$ (see [18,19] for details). Equation (1) shows that the potential field is generated by a distribution of sources and doublets over the bodies, along with doublet distributions over the wake surfaces. However, using the boundary element method for the numerical solution of this equation causes instabilities to arise when wake panels come too close to or impinge on the body surfaces [15]. Thus, this formulation cannot be applied as it is to examine the problem under consideration.

The boundary integral approach proposed in [15] overcomes this limitation. It introduces the decomposition of the potential field into an incident field φ_I and a scattered field φ_S. The scattered potential is generated by sources and doublets over the body surfaces and by doublets over portions of the wakes that are very close to the trailing edges from which they emanated (near wakes $S_W^{w,N}$ and $S_W^{p,N}$). The incident potential is generated by the doublets over the complementary wake regions that compose the far wakes $S_W^{w,F}$ and $S_W^{p,F}$ (see Fig. 1 for a rotor blade wake). These are the wake portions that may come in contact with other body surfaces. The scattered potential is discontinuous across $S_W^{w,N}$ and $S_W^{p,N}$, whereas the incident potential is discontinuous across $S_W^{w,F}$ and $S_W^{p,F}$. Hence, as demonstrated in [15], for $\varphi=\varphi_I+\varphi_S$ the scattered potential is obtained by

$$\varphi_S(\mathbf{x},t)=\int_{S_B^w\cup S_B^p}\left[G(\chi-\chi_I)-\varphi_S\frac{\partial G}{\partial n}\right]\mathrm{d}S(\mathbf{y})-\int_{S_W^{w,N}\cup S_W^{p,N}}\Delta\varphi_S\frac{\partial G}{\partial n}\,\mathrm{d}S(\mathbf{y}) \quad (2)$$

where $\chi=\mathbf{v}\cdot\mathbf{n}$ and $\chi_I=\mathbf{u}_I\cdot\mathbf{n}$, with the velocity induced by the far wake, $\mathbf{u}_I$, given by

$$\mathbf{u}_I(\mathbf{x},t)=\nabla\varphi_I(\mathbf{x},t)=-\nabla\int_{S_W^{w,F}\cup S_W^{p,F}}\Delta\varphi_S(\mathbf{y}_W^{\mathrm{TE}},t-\vartheta)\frac{\partial G}{\partial n}\mathrm{d}S(\mathbf{y}) \quad (3)$$

The incident potential affects the scattered potential through the induced-velocity term χ_I, and, in turn, the scattered potential affects the incident potential by its trailing-edge discontinuity that is convected along the wake and yields the intensity of the doublet distribution over the far wake.

Obtaining the discrete form of Eq. (3) by using N panels over the far wakes and recalling the vortex-doublet equivalence, the incident velocity field may be evaluated through the following expression:

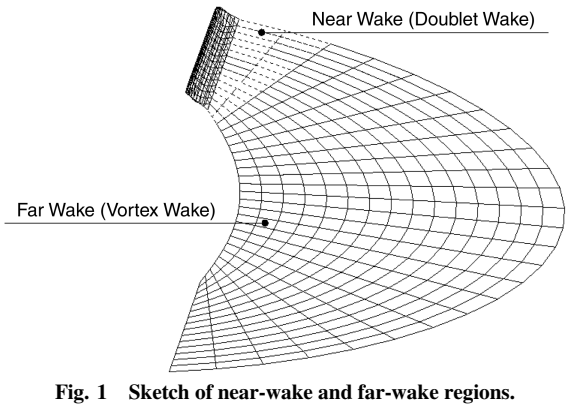

Fig. 1 Sketch of near-wake and far-wake regions.

$$\mathbf{u}_I(\mathbf{x},t) \approx -\sum_{n=1}^{N} \Delta\varphi_S(\mathbf{y}_{W_n}^{\mathrm{TE}}, t-\vartheta_n) \int_{C_n} \nabla_{\mathbf{x}} G \times \mathrm{d}\mathbf{y} \tag{4}$$

where C_n denotes the contour line of the nth far-wake panel, $\mathbf{y}_{W_n}^{\mathrm{TE}}$ is the trailing-edge position where the wake material point currently in $\mathbf{y}_{W_n}$ emanated at time $t-\vartheta_n$, and $\nabla_{\mathbf{x}}$ denotes gradient operator with respect to the variable $\mathbf{x}$. This equation represents the velocity field given by the Biot–Savart law applied to the vortices having the shape of the far-wake panel contours and intensity $\Delta\varphi_S(\mathbf{y}_{W_n}^{TE}, t-\vartheta_n)$. Equation (4) is applied to evaluate both the term χ_I in Eq. (2) and, once extended to the whole wake, to evaluate the velocity field in the free-wake distortion analysis, if required.

The final step of the formulation consists of introducing in Eq. (4) a finite-thickness vortex model that ensures a regular distribution of the induced velocity within the vortex core and thus a stable and regular solution even in body–vortex impact conditions [15] (it is worth recalling that only the far wake may experience such events). The description of the wake influence through the use of finite-core vortices is a way to also include diffusivity and vortex-stretching effects that otherwise would not be taken into account in a potential-flow aerodynamic formulation (see [20,21] for details on this issue).

Equation (2) is solved numerically by boundary elements (i.e., by dividing $S_B^w \cup S_B^p$ and $S_W^{w,N} \cup S_W^{p,N}$ into quadrilateral panels), assuming φ_S, χ, χ_I, and $\Delta\varphi_S$ to be piecewise constant [zeroth-order boundary element method (BEM)] and imposing that the equation be satisfied at the center of each body element (collocation method) [15].

Once the potential field is known, the Bernoulli theorem yields the pressure distribution and hence blade loads may be evaluated through integration [15].

III. Wing–Proprotor Aeroelastic Model

The aeroelastic formulation is obtained by combining the aerodynamic loads given by the solver outlined above with the equations governing the dynamics of the wing–proprotor system. Beamlike models are applied to describe the structural dynamics of both wing and proprotor blades.

Blade equations are based on the nonlinear bending-torsion formulation presented in [22], that is valid for straight, slender, homogeneous, isotropic, nonuniform, twisted blades, undergoing moderate displacements. For x denoting a spanwise coordinate along the undeformed blade, the components of the displacement of the elastic axis in the plane of cross section, lead lag $v_b(x,t)$, and flap $w_b(x,t)$, (with v_b lying in the plane of rotation), along with the torsion of the cross section, $\phi_b(x,t)$, about the deformed elastic axis, are governed by the following three dimensionless integro-partial differential equations [22]:

$$\begin{aligned}&[(\Lambda_2^b - \Lambda_{21}^b \sin^2\theta_b) v_b'']'' + \left[\frac{\Lambda_{21}^b}{2} w_b'' \sin(2\theta_b)\right]'' \\ &+ [\Lambda_{21}^b(\phi_b w_b'' \cos(2\theta_b) - \phi_b v_b'' \sin(2\theta_b))]'' - [e_A T \cos(\theta_b+\phi_b)]'' \\ &- (T v_b')' = L_v^b(\mathbf{x}_b,\mathbf{x}_w) + p_y(\mathbf{x}_b,\mathbf{x}_w) - q_z'(\mathbf{x}_b,\mathbf{x}_w)\end{aligned} \tag{5}$$

$$\begin{aligned}&[(\Lambda_1^b + \Lambda_{21}^b \sin^2\theta_b) w_b'']'' + \left[\frac{\Lambda_{21}^b}{2} v_b'' \sin(2\theta_b)\right]'' \\ &+ [\Lambda_{21}^b(\phi_b v_b'' \cos(2\theta_b) + \phi_b w_b'' \sin(2\theta_b))]'' - [e_A T \sin(\theta_b+\phi_b)]'' \\ &- (T w_b')' = L_w^b(\mathbf{x}_b,\mathbf{x}_w) + p_z(\mathbf{x}_b,\mathbf{x}_w) + q_y'(\mathbf{x}_b,\mathbf{x}_w)\end{aligned} \tag{6}$$

$$\begin{aligned}&\Lambda_{21}^b[(w_b''^2 - v_b''^2)\sin\theta_b\cos\theta_b + v_b'' w_b'' \cos(2\theta_b)] - (\kappa_b\phi_b')' \\ &- [K_b^2 T(\phi_b+\theta_b)']' - e_A T(w''\cos\theta_b - v''\sin\theta_b) \\ &= M_\phi^b(\mathbf{x}_b,\mathbf{x}_w) + q_x(\mathbf{x}_b,\mathbf{x}_w) + v_b' q_y(\mathbf{x}_b,\mathbf{x}_w) + w_b' q_z(\mathbf{x}_b,\mathbf{x}_w)\end{aligned} \tag{7}$$

where the tension T is given by

$$T = \int_x^1 p_x(\mathbf{x}_b,\mathbf{x}_w)\,\mathrm{d}\bar{x} \tag{8}$$

and $'$ denotes differentiation with respect to the dimensionless spanwise coordinate. In the equations above, dimensionless lengths are related to the blade radius R whereas dimensionless time coincides with blade azimuth position. The bending equations (5) and (6) have been obtained by dividing by the factor $m_0^b\Omega^2 R$, whereas the torsion equation (7) is the result of division by the factor $m_0^b\Omega^2R^2$, with m_0^b denoting the reference blade mass per unit length and Ω denoting the angular velocity of the blade; in addition, $\Lambda_{21}^b = \Lambda_2^b - \Lambda_1^b$, and e_A denotes the distance between tensile axis and elastic axis [22,23]. The blade loading terms given by section inertial forces p_x, p_y, and p_z; section inertial moments q_x, q_y, and q_z; and section aerodynamic loads L_v^b, L_w^b, and M_ϕ^b are functions of the blade section degrees of freedom $\mathbf{x}_b = \{v_b, w_b, \phi_b\}$ but also are affected by the elastic deformation of the wing, described here in terms of bending displacements v_w and w_w and torsion ϕ_w ($\mathbf{x}_w = \{v_w, w_w, \phi_w\}$). These coupling terms represent the wing influence on proprotor dynamics and are obtained by including in the blade kinematics the effects of the motion of the wing section linked to the pylon. Note that in Eqs. (5–7) blade precone angle, hinge offset, torque offset, and mass offset, if present, would appear in the description of the distributed inertial loads.

The equations governing wing dynamics are similar to those presented for the proprotor blades. In this case, however, because of the smaller elastic displacements experienced by wings with respect to rotor blades, only first-order terms are retained in the formulation. Additional forcing terms appear because of the loads transmitted by the proprotor hub and from pylon inertial effects. Specifically, for x denoting a spanwise coordinate, the equations governing the displacements of the wing elastic axis, $v_w(x,t)$ and $w_w(x,t)$, and torsion of the wing cross section, $\phi_w(x,t)$, read

$$\begin{aligned}&[(\Lambda_2^w - \Lambda_{21}^w \sin^2\theta_w) v_w'']'' + \left[\frac{\Lambda_{21}^w}{2} w_w'' \sin(2\theta_w)\right]'' + \bar{m}_w \ddot{v}_w \\ &- \bar{m}_w e \sin\theta_w \ddot{\phi}_w = L_v^w(v_w, w_w, \phi_w) + [V_x(\mathbf{x}_b,\mathbf{x}_w)\delta_p v_w']' \\ &+ V_y(\mathbf{x}_b,\mathbf{x}_w)\delta_p - [M_z(\mathbf{x}_b,\mathbf{x}_w)\delta_p]'\end{aligned} \tag{9}$$

$$\begin{aligned}&[(\Lambda_1^w + \Lambda_{21}^w \sin^2\theta_w) w_w'']'' + \left[\frac{\Lambda_{21}^w}{2} v_w'' \sin(2\theta_w)\right]'' + \bar{m}_w \ddot{w}_w \\ &+ \bar{m}_w e \cos\theta_w \ddot{\phi}_w = L_w^w(v_w, w_w, \phi_w) + [V_x(\mathbf{x}_b,\mathbf{x}_w)\delta_p w_w']' \\ &+ V_z(\mathbf{x}_b,\mathbf{x}_w)\delta_p + [M_y(\mathbf{x}_b,\mathbf{x}_w)\delta_p]'\end{aligned} \tag{10}$$

$$\begin{aligned}&-(\kappa_w\phi_w')' + \mu_w^2\ddot{\phi}_w - \bar{m}_w e \sin\theta_w \ddot{v}_w + \bar{m}_w e\cos\theta_w \ddot{w}_w \\ &= M_\phi^w(v_w, w_w, \phi_w) + [K_w^2 V_x(\mathbf{x}_b,\mathbf{x}_w)\delta_p(\phi_b+\theta_b)']' \\ &+ M_x(\mathbf{x}_b,\mathbf{x}_w)\delta_p + v_w' M_y(\mathbf{x}_b,\mathbf{x}_w)\delta_p + w_w' M_z(\mathbf{x}_b,\mathbf{x}_w)\delta_p\end{aligned} \tag{11}$$

where v_w is aligned with the tiltrotor longitudinal axis, $\Lambda_{21}^w = \Lambda_2^w - \Lambda_1^w$ and $\bar{m}_w = m_w/m_0^w$ is the ratio between mass distribution and reference mass distribution, whereas e denotes the dimensionless mass offset. In these equations, the wing semispan L_w has been used as the reference length and $\dot{}$ denotes the dimensionless time derivative. As mentioned above, in addition to the aerodynamic loads L_v^w, L_w^w, and M_ϕ^w, wing dynamics is also forced by shear forces V_x, V_y, and V_z and moments M_x, M_y, and M_z, transmitted by the pylon/proprotor system at the wing section x_p, where the pylon is located [$\delta_p = \delta(x-x_p)$, with δ denoting the Dirac delta function]. The proprotor loads are obtained as integration of aerodynamic and inertial forces acting over the blades.

Equations (5–7) and (9–11) demonstrate that blade dynamics equations and wing dynamics equations are strongly coupled and have to be solved simultaneously to determine the dynamics of the wing/pylon/proprotor system. If the proprotor is linked to the pylon

through a gimbal, then the gimbal degrees of freedom $\beta_c(t)$ and $\beta_s(t)$ have to be included in the description of the blade kinematics, and the following gimbal equations added to the set of dynamics equations [2]:

$$\ddot{\beta}_c - C_g\dot{\beta}_c + 2\dot{\beta}_s + K_g\beta_c = -M_y^g \tag{12}$$

$$\ddot{\beta}_s + C_g\dot{\beta}_s - 2\dot{\beta}_c + K_g\beta_s = M_x^g \tag{13}$$

For I_b denoting the blade moment of inertia and N the number of blades, stiffness and damping coefficients in the equations above are such that gimbal hub spring and damper in the nonrotating frame are given by $NI_b\Omega^2K_g/2$ and $NI_b\Omega C_g/2$, respectively, and M_x^g and M_y^g are the dimensionless moments forcing gimbal motion. These moments are given by contributions from proprotor aerodynamic loads (depending on wing, gimbal, and blade Lagrangian variables) and from proprotor inertial loads due to wing and blade deformation (in this model the wing deformation drives the shaft motion).

Equations (5–7) and (9–11) [with inclusion of Eqs. (12) and (13), if needed] coupled with the aerodynamic solver yield the wing–proprotor aeroelastic model to be integrated. To this aim, the space discretization of both wing and proprotor blade equations is performed through the Galerkin method, starting from elastic deformations described as a linear combination of suitable linearly independent shape functions (in this paper, the natural modes of a cantilever beam have been applied). The resulting aeroelastic system consists of a set of nonlinear ordinary differential equations of the type

$$\mathbf{M}(t)\ddot{\mathbf{q}} + \mathbf{C}(t)\dot{\mathbf{q}} + \mathbf{K}(t)\mathbf{q} = \mathbf{f}_{\text{str}}^{\text{nl}}(t,\mathbf{q}) + \mathbf{f}_{\text{aer}}(t,\mathbf{q}) \tag{14}$$

where $\mathbf{q}$ denotes the vector of the Lagrangian coordinates of wing and blades (with the addition of gimbal degrees of freedom, if present), and $\mathbf{M}$, $\mathbf{C}$, and $\mathbf{K}$ are time-periodic, mass, damping, and stiffness matrices representing the linear structural terms. Nonlinear structural contributions are collected in $\mathbf{f}_{\text{str}}^{\text{nl}}(t,\mathbf{q})$, and $\mathbf{f}_{\text{aer}}(t,\mathbf{q})$ collects the generalized aerodynamic forces (with inclusion of aerodynamic loads transmitted to the wing by the proprotor).

This work deals with tiltrotors in uniform rectilinear motion, during which wing and proprotor blades are subject to steady periodic deformations: the blade passage frequency (N/rev, for an N-bladed proprotor) is the fundamental frequency of wing response, whereas the fundamental frequency of proprotor blade response is the rotor frequency of revolution. Thus, the solution of Eq. (14) and hence the prediction of the vibratory loads is based on a harmonic balance approach. This is a methodology suitable for the analysis of asymptotic solutions of differential equations (as time goes to infinity) forced by periodic terms, as in the present problem. Indeed, steady periodic aerodynamic loads are present in any flight condition: in helicopter mode these arise mainly because of polar flow-asymmetry on proprotor blades and cyclic controls, whereas in airplane mode they come from the aerodynamic interaction between wing and proprotor (in conversion settings both sources of periodic loads are present). The harmonic balance solution consists of the following:

1) Express left-hand side and right-hand side of Eq. (14) in terms of Fourier series.

2) Equate the resulting coefficients.

3) Solve the corresponding algebraic set of equations in terms of the unknown Fourier coefficients of the Lagrangian coordinates of the problem. Note that, the harmonic balance solution of Eq. (14) requires an iterative procedure.

IV. Numerical Results

The numerical investigation starts with the validation of the unsteady BEM formulation for the prediction of wing–proprotor aerodynamics. Then results of the analysis of vibratory loads arising in airplane-mode and helicopter-mode configurations of a tiltrotor in uniform level-flight conditions will be presented.

A. Validation of BEM Aerodynamic Solver

The configuration considered is the right propeller/nacelle/half-wing test model that has been investigated experimentally within the Brite EuRam research project PROPWING and is also presented in [12,13]. The propeller has four blades with radius $R = 0.425$ m and NACA 64A408 airfoil sections (chord length and twist distributions are given in [12,24]). The half-wing is untwisted and has RA18-43N1L1 airfoil sections, length $L_w = 1.0$ m and constant chord $c = 1.02$ m [13]. The results presented in the following concern the airplane-mode configuration, with freestream velocity $V = 17.2$ m/s and propeller rotating clockwise (seen from downstream) with angular velocity $\Omega = 1362$ RPM (see [13] for further details). In this condition, periodic pressure distributions arise on the wing surface because of both the close blade passages and the impact with the wake vortices released by the lifting propeller. Thus, the validation of the BEM solver is accomplished both in terms of wing section mean pressure distributions and in terms of wing local pressure–time histories. Note that, although the oscillatory loads are of more interest in this work, mean pressure distributions are also examined because they are related to trim and performance analysis applications and contribute to give a more complete view of the capability of the numerical tool to capture the aerodynamic solution.

Figure 2 shows the comparison between measured and calculated mean pressure coefficient, $\bar{c}_p$, along the upper side of the wing section located at a distance of 0.5 m from the wing root, where numerical predictions are most critical in that it is very close to the region of blade tip-vortex passage (it is placed approximately behind the rotor-disk edge). The mean pressure coefficient along the lower side of the same wing section is illustrated in Fig. 3. In addition to the results obtained through the present approach, Figs. 2 and 3 also depict the numerical predictions presented in [12] that have been obtained through a potential-flow formulation different from that presented here. On the upper side of the section the predictions from the present formulation are in good agreement with the experimental ones, showing an overall correlation that seems to be slightly better than that from [12]. On the lower side, similarly to [12], the predictions from the present approach capture the presence of a suction peak close to the leading edge, but are affected by some overestimation; however, after the first 10% portion of the section chord the present calculations are in excellent agreement with the experimental data, also predicting correctly the almost-constant pressure distribution in $0.1 \le x/c \le 0.5$ (with $x$denoting here chordwise coordinate from leading edge).

Next, a wing section located out of the propeller wake and a wing section located inside the region where the propeller wake is convected are considered. The first one is 0.3 m distant from the wing root, close to the rotor-disk edge. The corresponding results concerning the mean pressure coefficient over upper and lower sides are shown in Figs. 4 and 5, respectively. In this case, present predictions are in very good agreement with the measured data on both regions, with the lower-side suction peak well captured both in location and intensity, whereas results from [12] show significant discrepancies

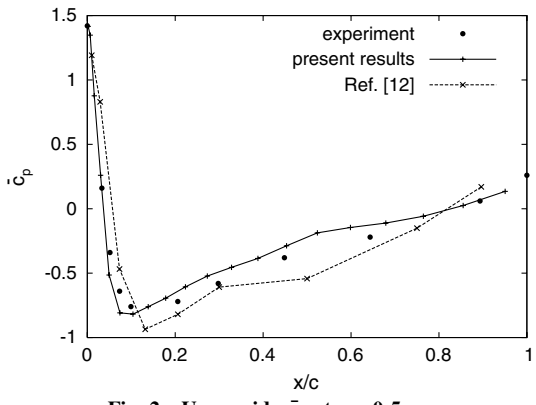

Fig. 2 Upper side, $\bar{c}_p$ at $y = 0.5$ m.

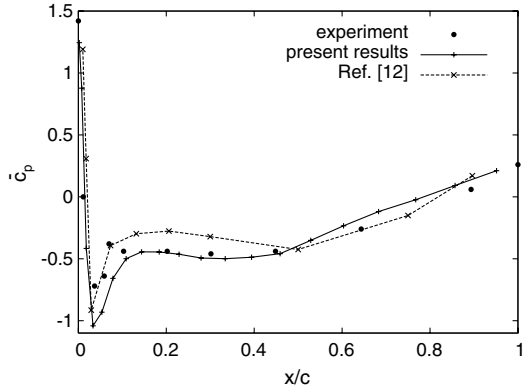

Fig. 3 Lower side, $\bar{c}_p$ at $y = 0.5$ m.

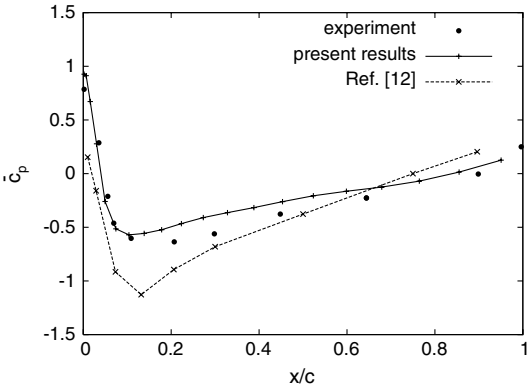

Fig. 4 Upper side, $\bar{c}_p$ at $y = 0.3$ m.

with respect to them. The wing section within the rotor disk is located 0.7 m from the wing root, very close to the nacelle. The distributions of the mean pressure coefficient along upper and lower sides of it are given, respectively, in Figs. 6 and 7. For this section, present results concerning the upper side correlate well with the experiments, whereas an overestimation of the leading-edge pressure peak is observed in the lower side, followed by a satisfactory prediction of the pressure distribution for $x/c > 0.15$ (an overestimation of the leading-edge suction peak similarly appears in [12]). The significant discrepancy on the lower-side leading edge could be due to the difficulty in capturing the interaction effects (dominated by viscosity) between propeller hub, wing and nacelle arising in the wing–nacelle connection region.

Then, predictions concerning pressure–time histories over the wing surface are presented and compared with experimental data produced within the Brite EuRam research project PROPWING (see also [12,13]). Figure 8 shows the comparison for five transducers located on the upper side of the wing at the section closest to the tip-vortex passage region, where the experiments have measured the

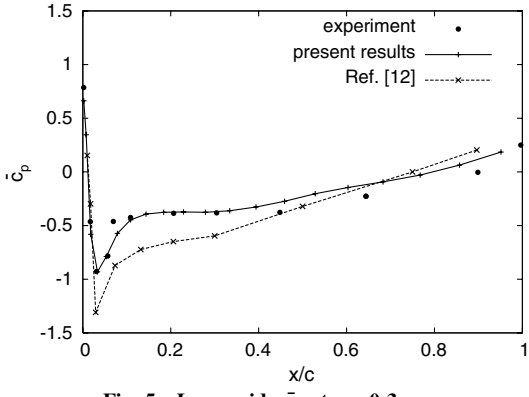

Fig. 5 Lower side, $\bar{c}_p$ at $y = 0.3$ m.

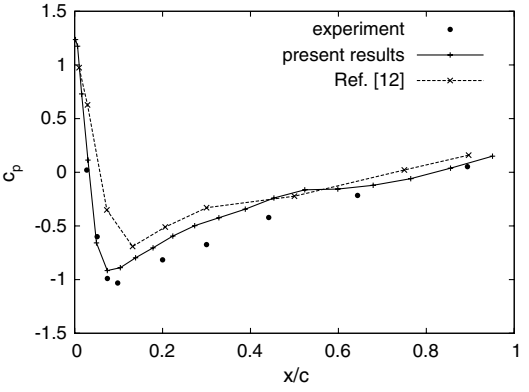

Fig. 6 Upper side, $\bar{c}_p$ at $y = 0.7$ m.

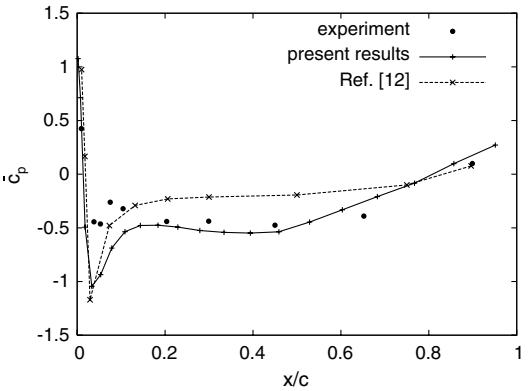

Fig. 7 Lower side, $\bar{c}_p$ at $y = 0.7$ m.

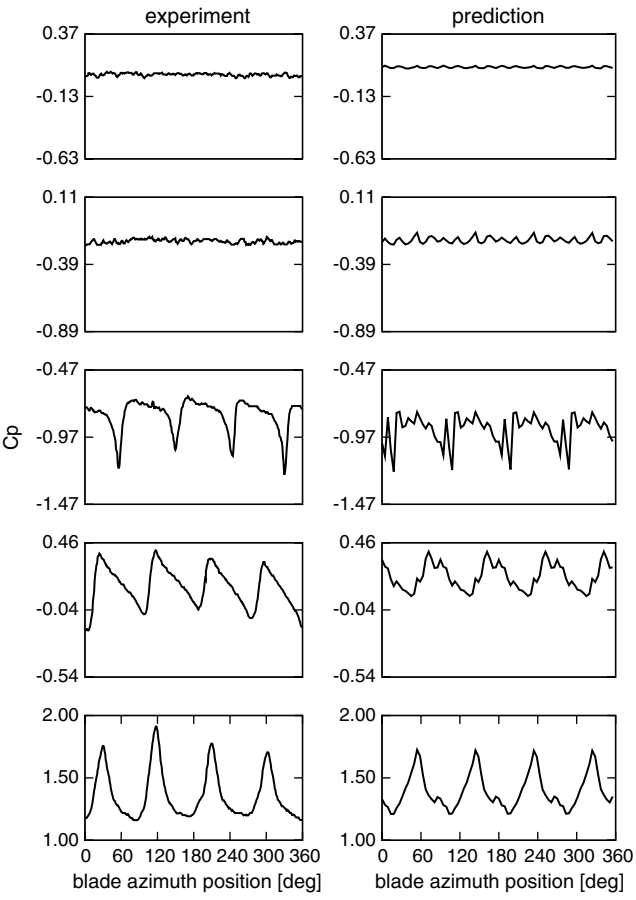

Fig. 8 Upper side, c_p time histories at $y = 0.5$ m. Chordwise positions are $x/c = 0.9$, 0.65, 0.1, 0.024, and 0, starting from top pictures.

most significant oscillatory behavior of pressure. Pictures at the bottom of the figure concern the transducer closer to the leading edge (indicated in [12,13] as transducer number 1), pictures at the top concern the trailing-edge transducer (indicated in [12,13] as transducer number 10), and the other pictures concern transducers located along the chord (specifically, numbers 2, 5, and 9 in [12,13]). Although a higher frequency content is observed in the predictions related to the transducer number 5 and a phase shift of about 30° is present (probably because of the difference between the numerical and experimental initial acquisition times), numerical results capture the regions with the highest pressure oscillations (with a satisfactory prediction of the peak-to-peak values), along with the attenuation of pressure oscillation amplitude that occurs moving from leading-edge to trailing-edge positions. Numerical predictions show that along the lower side of the same wing section the 4/rev pressure oscillations are negligible, and this is confirmed by the measurements, as illustrated in Fig. 9 (concerning transducers number 11, 12, 15, 19, and 20 in [12,13], from top to bottom). The pressure oscillations in Figs. 8 and 9 are due to the interaction between propeller blade tip vortices and wing. Indeed, numerical simulation predicts the absence of oscillations at sections outside of the wing region impinged by propeller wake, as well as the presence of very small oscillations at wing sections inside the propeller wake region that are not close to tip-vortex passage. This is confirmed by the experimental measurements as demonstrated, for instance, in Figs. 10 and 11, which depict, respectively, pressure–time histories on the upper and lower sides of the section located 0.7 m from the wing root. However, in addition to the discrepancies in the mean value of pressure already observed in Fig. 7, these figures show a slightly overestimated prediction of the pressure oscillations close to the leading edge at the lower side of the section examined (also these small discrepancies could be due to interaction viscous effects between propeller hub, wing and nacelle, not considered here).

B. Analysis of Vibratory Loads

The analysis of the vibratory loads transmitted by the wing–proprotor system to the airframe has been performed by considering the wing–proprotor model examined in [1]. The wing considered has length $L_w = 5.092$ m and chord $c = 1.58$ m, and the three-bladed wing proprotor has radius $R = 3.82$ m (see [1] for further details on the geometrical and structural properties). The predictions of vibratory loads presented in the following are given in nondimensional form; specifically, wing–root forces and moments have been divided, respectively, by the factors $m_0^w \Omega^2 L_w^2$ and $m_0^w \Omega^2 L_w^3$, with $m_0^w = 32.5$ kg/m, whereas proprotor hub forces and moments have been divided, respectively, by the factors $m_0^b \Omega^2 R^2$ and $m_0^b \Omega^2 R^3$, with $m_0^b = 7.64$ kg/m.

First, the wing–proprotor has been examined in an airplane-mode configuration. In this condition, the flight velocity considered is $V = 128.5$ m/s, whereas the proprotor angular velocity is $\Omega = 458$ RPM (corresponding to advance ratio $\mu = 0.7$). The wing angle of attack is equal to 3° and the proprotor axis is aligned with the freestream. Cyclic pitch control is not present, and the steady misalignment between proprotor axis and freestream velocity due to wing elastic deformation and gimbal deflection is very small; hence, negligible vibratory loads would be predicted without including wing–proprotor interaction effects in the aerodynamic simulation model. Specifically, aerodynamic unsteady loads arise on proprotor blades because of the flowfield asymmetry due to the presence of the wing, whereas aerodynamic unsteady loads over the wing arise because of the impact between proprotor wake and wing surface. Figure 12 depicts the 3/rev vibratory loads given by the numerical prediction as those transmitted by the wing to the airframe at the shear center of the root section. It compares the total loads with those obtained neglecting the contribution from wing aerodynamics (the load components are given with respect to a hub frame of reference having the x axis aligned with the freestream and the y axis directed

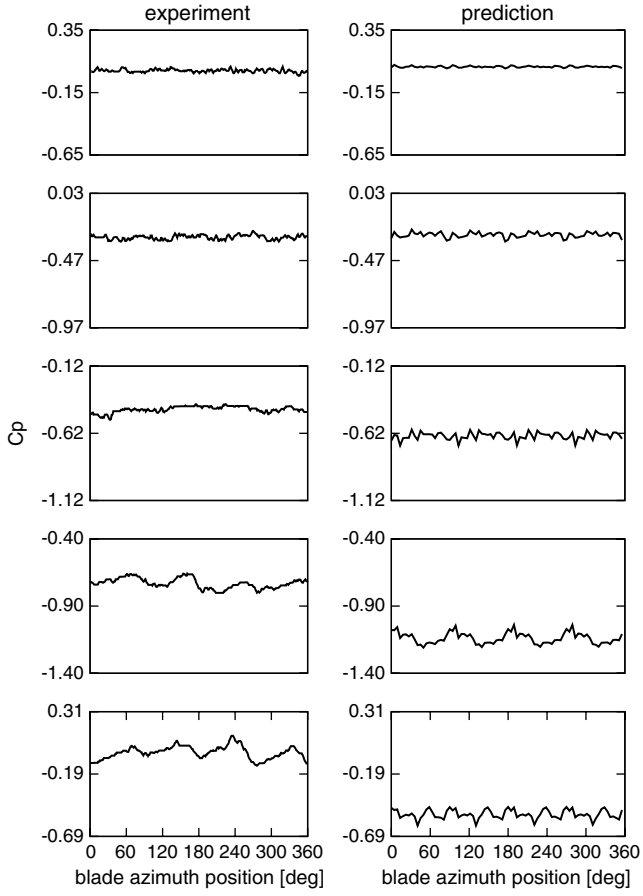

Fig. 9 Lower side, c_p time histories at $y = 0.5$ m. Chordwise positions are $x/c = 0.9$, 0.65, 0.2, 0.024, and 0.012, starting from top pictures.

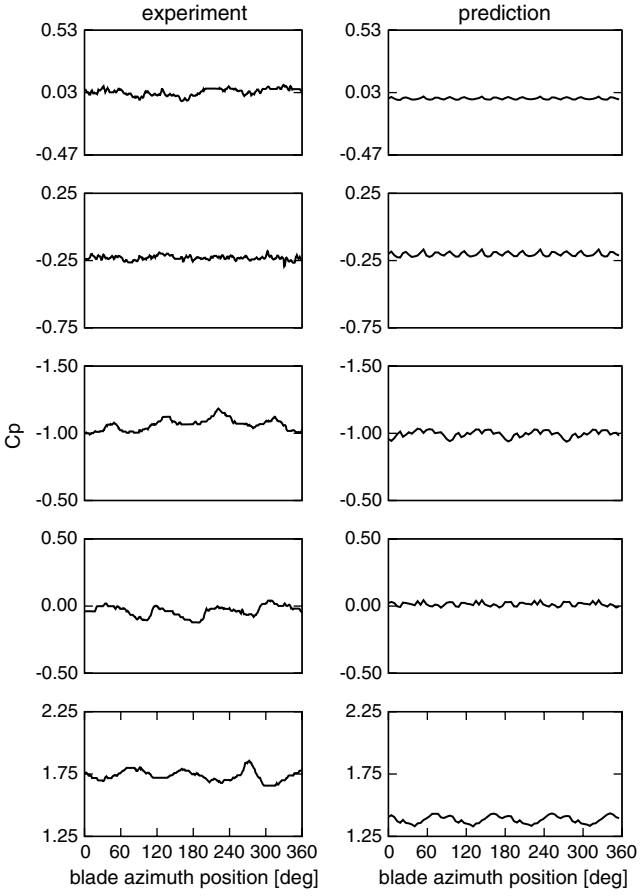

Fig. 10 Upper side, c_p time histories at $y = 0.7$ m. Chordwise positions are $x/c = 0.9$, 0.65, 0.1, 0.024, and 0, starting from top pictures.

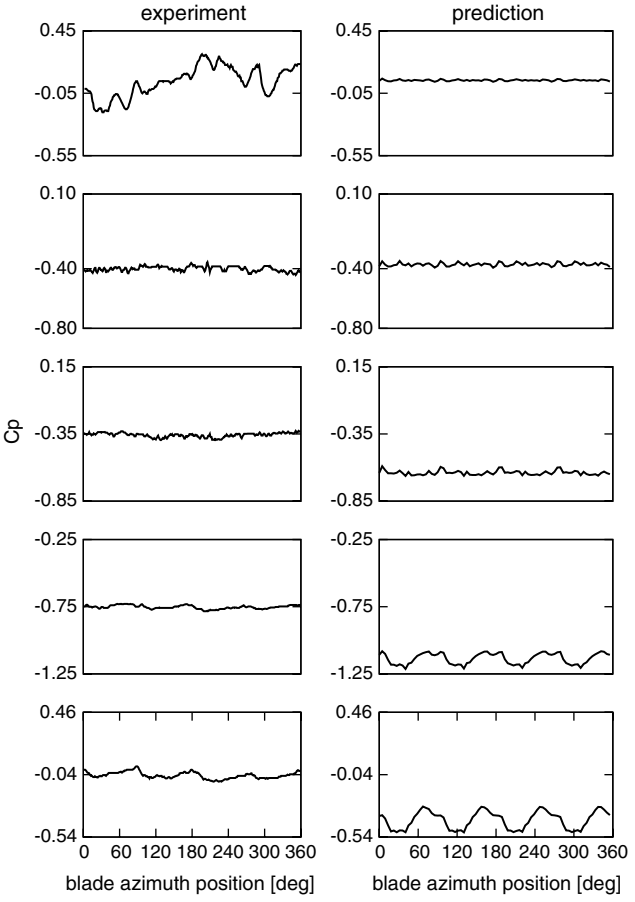

Fig. 11 Lower side, c_p time histories at $y = 0.7$ m. Chordwise positions are $x/c = 0.9$, 0.65, 0.2, 0.024, and 0.012, starting from top pictures.

along the span). These results show that the unsteady aerodynamic loads arising over the wing because of the impact with proprotor blade vortices slightly affect shear loads and moment M_z but have a significant effect on bending moment M_x and torsional moment M_y. Because, as mentioned above, these vibratory loads are generated by the aerodynamic interaction between wing and proprotor, they strongly depend on the geometry of the wing–propeller configuration (particularly, on the relative positions) and it is of interest to examine how important is the effect of system elastic deformations. The results of this analysis are given in Figs. 13 and 14, which present, respectively, the 3/rev vibratory loads predicted at the proprotor hub taking into account only blade aerodynamics loads and the 3/rev vibratory loads due to wing aerodynamics predicted at the wing root (the load components at the hub are given with respect to a frame of reference with the y axis aligned with the span and the z axis aligned

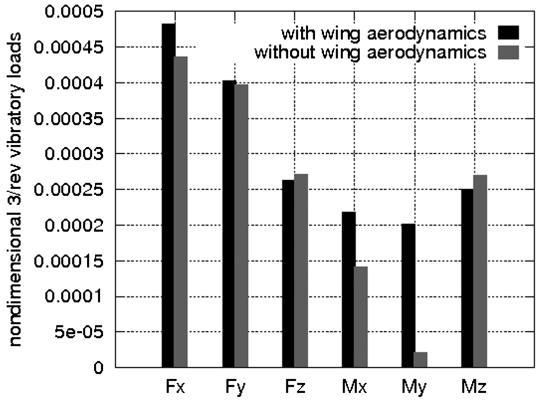

Fig. 12 Vibratory loads at the wing root in airplane mode.

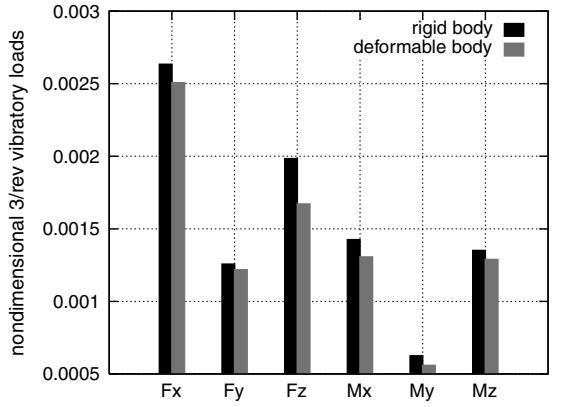

Fig. 13 Vibratory loads at the proprotor hub in airplane mode, because of blade aerodynamics.

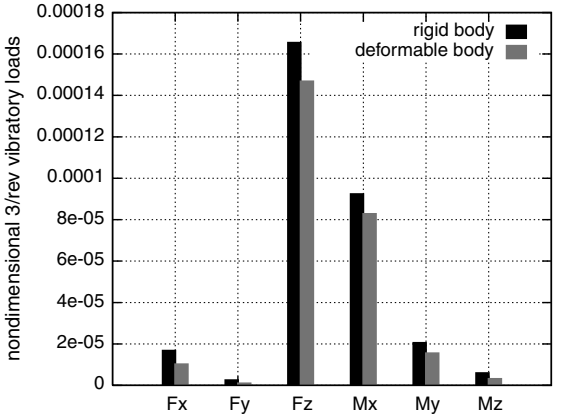

Fig. 14 Vibratory loads at the wing root in airplane mode, because of wing aerodynamics.

with the proprotor shaft). These figures compare the results from the complete aeroelastic analysis with those from rigid-body assumption. It is interesting to observe that the proprotor–wing aerodynamic loads seem to be weakly affected by elastic deformations and thereby their evaluation could be performed without taking into account coupling with structural dynamics. It is worth noting that, even in this case, the analysis of the structural dynamics forced by the aerodynamic action would be fundamental for the evaluation of the inertial component of vibratory loads. On the other hand, a crucial role is played by the aerodynamic model applied in the simulation tool. This fact is shown by Fig. 15, which depicts the comparison between the wing–root total vibratory loads computed by the aeroelastic tool based on the BEM solver presented in Sec. II and those obtained from the aerodynamic

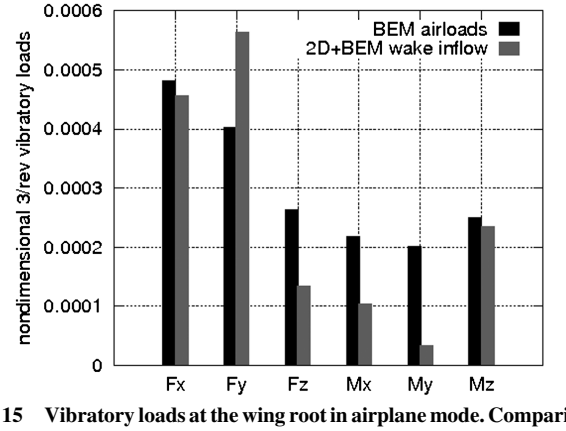

Fig. 15 Vibratory loads at the wing root in airplane mode. Comparison between predictions from two aerodynamic models.

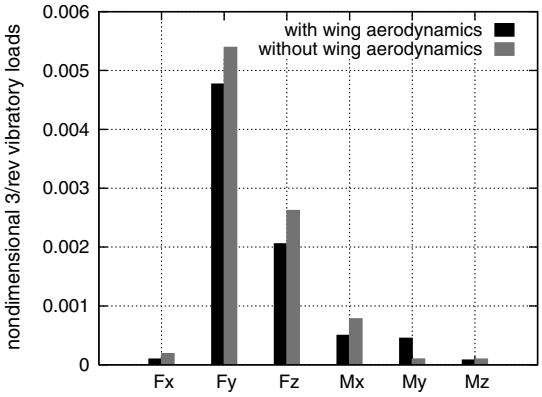

Fig. 16 Vibratory loads at the wing root in helicopter mode.

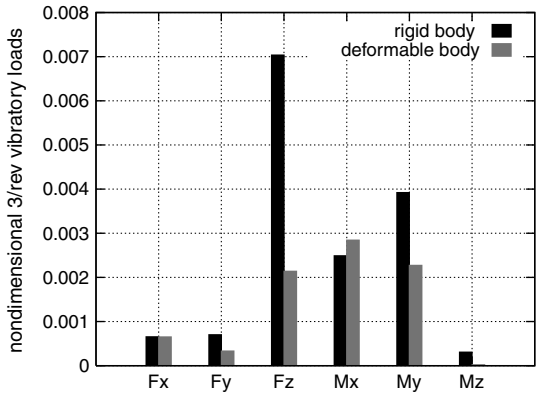

Fig. 17 Vibratory loads at the proprotor hub in helicopter mode, because of blade aerodynamics.

loads evaluated by the quasi-steady approximation of 2-D airfoil theories [25,26] combined with the velocity field induced by the complex wake structure (as given by the BEM solution). Indeed, it demonstrates that different aerodynamic models yield different vibratory load predictions (especially $F_z$bending moment M_x and torsion moment M_y in the case examined here) and therefore, in this kind of analysis, the application of an aerodynamic solver that is able to capture interaction effect as accurately as possible is recommended.

Then, such a numerical investigation on the prediction of vibratory loads has also been performed for the wing–proprotor system in helicopter configuration. Specifically, the wing proprotor has been examined at flight velocity $V = 30.84$ m/s, proprotor angular velocity $\Omega = 600$ RPM, and with the shaft having an inclination of

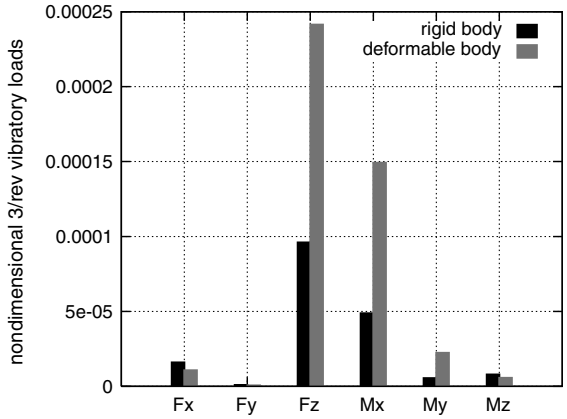

Fig. 18 Vibratory loads at the wing root in helicopter mode, because of wing aerodynamics.

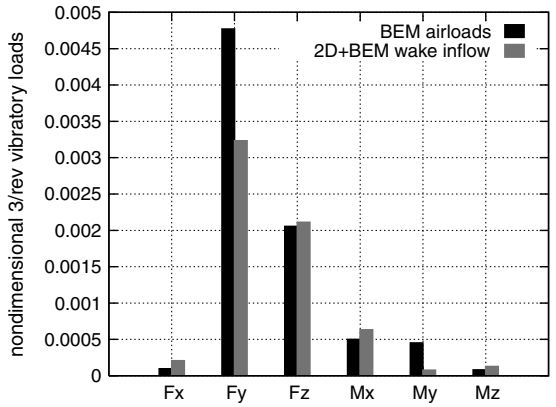

Fig. 19 Vibratory loads at the wing root in helicopter mode. Comparison between predictions from two aerodynamic models.

9 deg with respect to the vertical direction (the corresponding advance ratio is $\mu = 0.13$). Figure 16 shows the 3/rev vibratory loads predicted at the shear center of the wing–root section and compares the total loads with those obtained neglecting the contribution from wing aerodynamics. As expected, in this case the vibratory loads are much greater than those predicted in airplane-mode flight (mainly because proprotors operate with a large in-plane flight velocity component, under the action of blade cyclic pitch control and an axially asymmetric velocity field induced by the wake), whereas the contribution from the aerodynamic loads acting over the wing is negligible (no impact between proprotor wake and wing occurs and wing–proprotor interaction effects are weak). Figures 17 and 18 show, respectively, the 3/rev vibratory loads predicted at the proprotor hub from blade aerodynamics and the 3/rev vibratory loads predicted at the wing root from wing aerodynamics. These figures demonstrate that, contrary to what observed in airplane mode, in this flight condition, the vibratory aerodynamic loads arising over the proprotor blades and wing are heavily affected by their elastic deformation. Finally, the comparison between the wing–root vibratory loads computed through the BEM solver and those obtained from the aerodynamic model based on quasi-steady approximation of airfoil theories combined with the wake-induced velocity field is presented in Fig. 19. It shows that in the helicopter-mode configuration examined the simplified aerodynamic modeling (frequently used in helicopter applications) yields predictions that, with respect to the results obtained in airplane mode, in the overall are closer to those given by the 3-D unsteady aerodynamic solver. Nonetheless, significant discrepancies appear in the evaluation of side force F_y and torsion moment M_y.

V. Conclusions

A numerical methodology for the aerodynamic/aeroelastic analysis of wing–proprotor systems has been presented. The aerodynamic solver has been validated by correlation with experimental data available in the literature. The aeroelastic response has been evaluated in order to examine the vibratory loads transmitted to the tiltrotor airframe by the wing–proprotor system. The aerodynamic BEM formulation has been proven to be able to predict with very good accuracy the mean pressure distribution over the wing surface impinged by the proprotor wake. Some discrepancy with the experimental data appears at the lower-side leading-edge regions behind the rotor disk, close to the nacelle, because of wing–nacelle interaction effects dominated by viscosity, that are not included in the approach applied. In terms of pressure–time history, the aerodynamic solver has shown to be able to identify the regions along the span where pressure oscillations due to the impact between proprotor-wake tip vortex and wing surface are stronger, yielding a quite accurate prediction of the peak-to-peak values. In addition, it satisfactorily predicts the attenuation of the pressure fluctuation that occurs in these regions, moving from the leading edge to the trailing

edge of the sections. In the overall, the aerodynamic formulation presented captures with satisfactory accuracy the complex unsteady interaction effects arising between wing and proprotors, and thus it seems to be suitable for applications in the aeroelastic analysis of tiltrotor configurations. The numerical investigation on the vibratory loads in airplane-mode configuration, where the wing–proprotor aerodynamic interference plays a crucial role, has shown that a significant contribution is given by the proprotor-wake impingement on the wing surface. Hence, an aerodynamic solver is suitable for this kind of analysis only if it is able to capture accurately the effects from body–vortex impacts. A remarkable sensitivity of the predicted vibratory loads on the aerodynamic model applied has been proven. In addition, the numerical predictions have also demonstrated that in airplane-mode flight the aerodynamic interaction effects that generate the vibratory loads are weakly affected by wing and proprotor blade elastic deformations. Thereby, a rigid-body analysis may be used to get a quite accurate, faster estimation of the vibratory aerodynamic loads. In helicopter-mode configuration, the vibratory levels are higher than those in airplane mode, and the wing aerodynamic contribution to wing–root vibratory loads is almost negligible (wing–proprotor aerodynamic interaction effects are weak). Wing–proprotor elastic deformations have been proven to affect heavily the vibratory aerodynamic loads arising over the wing and proprotor blades, and hence an accurate vibratory aerodynamic analysis can be obtained only if combined with the structural dynamics analysis. Finally, in helicopter-mode flight, it has been shown that an aerodynamic model based on a quasi-steady approximation of airfoil theories yields predictions that, although strong wing–proprotor aerodynamic interactions are absent, present some significant differences with respect to those obtained by the 3-D unsteady aerodynamic solver. However, in the overall, their quality is such that they might conveniently be used for fast, rough estimation of the vibratory loads.

Acknowledgment

Experimental data concerning pressure distribution over the wing–proprotor system examined here have been obtained from the database produced within the Brite EuRam research project PROP funded by the European Union, contract AERO-90-0029.

References

[1] Johnson, W., "Dynamics of Tilting Proprotor Aircraft in Cruise Flight," NASA TN D-7677, May 1974.

[2] Johnson, W., "Analytical Model for Tilting Proprotor Aircraft Dynamics, Including Blade Torsion and Coupled Bending Modes, and Conversion Mode Operation," NASA TM X-62,369, Aug. 1974.

[3] Johnson, W., "Analytical Modeling Requirements for Tilting Proprotor Aircraft Dynamics," NASA TN D-8013, July 1975.

[4] Nixon, W. M., "Aeroelastic Response and Stability of Tiltrotors with Elastically-Coupled Composite Rotor Blades," Ph.D. Thesis, Univ. of Maryland, College Park, MD, 1993.

[5] Srinivas, V., and Chopra, I., "Formulation of a Comprehensive Aeroelastic Analysis for Tilt-Rotor Aircraft," *Journal of Aircraft*, Vol. 35, No. 2, 1998, pp. 280–287. doi:10.2514/2.2296

[6] Quaranta, G., Masarati, P., Lanz, M., Ghiringhelli, G. L., Mantegazza, P., and Nixon, W. M., "Dynamic Stability of Soft-In-Plane Tiltrotors by Parallel Multibody Analysis," *Proceedings of the 26th European Rotorcraft Forum*, The Hague, The Netherlands, 2000, pp. 60.1–60.9.

[7] Nixon, W. M., Kvaternik, R. G., and Settle, T. B., "Tiltrotor Vibration Reduction Through Higher Harmonic Control," *Journal of the American Helicopter Society*, Vol. 43, No. 3, 1998, pp. 235–245. doi:10.4050/JAHS.43.235

[8] Schillings, J., and Reinesch, R., "The Effect of Airframe Aerodynamics on V-22 Rotor Loads," *Journal of the American Helicopter Society*, Vol. 34, No. 1, 1989, pp. 26–33. doi:10.4050/JAHS.34.26

[9] Witkowski, D., Lee, A., and Sullivan, J., "Aerodynamic Interaction Between Propellers and Wings," *Journal of Aircraft*, Vol. 26, No. 9, 1989, pp. 829–836. doi:10.2514/3.45848

[10] Ardito Marreta, R. M., Daví, G., Milazzo, A., and Lombardi, G., "Wing Pitching and Loading with Propeller Interference," *Journal of Aircraft*, Vol. 36, No. 2, 1999, pp. 468–471. doi:10.2514/2.2455

[11] Fratello, G., Favier, D., and Maresca, C., "Experimental and Numerical Study of the Propeller/Fixed Wing Interaction," *Journal of Aircraft*, Vol. 28, No. 6, 1991, pp. 365–373. doi:10.2514/3.46036

[12] Benneceur, S., "Contribution à l'Étude des Interactions Aérodynamiques sur un Avion-Convertible (Configuration Hélice/Nacelle/Demi-Aile)," Ph.D., Thesis, Université d'Aix-Marseille II, Marseille, France, 1995 (in French).

[13] Chiaramonte, J. Y., Favier, D., Maresca, C., and Benneceur, S., "Aerodynamic Interaction Study of the Propeller/Wing Under Different Flow Configuration," *Journal of Aircraft*, Vol. 33, No. 1, 1996, pp. 46–53. doi:10.2514/3.46901

[14] Veldhuis, L. L. M., "Propeller Wing Aerodynamic Interference," Ph.D. Thesis, Delft Univ. of Technology, Delft, The Netherlands, 2005.

[15] Gennaretti, M., and Bernardini, G., "Novel Boundary Integral Formulation for Blade-Vortex Interaction Aerodynamics of Helicopter Rotors," *AIAA Journal*, Vol. 45, No. 6, 2007, pp. 1169–1176. doi:10.2514/1.18383

[16] Bernardini, G., Serafini, J., Ianniello, S., and Gennaretti, M., "Assessment of Computational Models for the Effect of Aeroelasticity on BVI Noise Prediction," *International Journal of Aeroacoustics*, Vol. 6, No. 3, 2007, pp. 199–222. doi:10.1260/147547207782419570

[17] Gennaretti, M., and Bernardini, G., "Aeroelastic Response of Helicopter Rotors Using a 3-D Unsteady Aerodynamic Solver," *The Aeronautical Journal*, Vol. 110, No. 1114, 2006, pp. 793–801.

[18] Morino, L., "A General Theory of Unsteady Compressible Potential Aerodynamics," NASA CR-2464, 1974.

[19] Morino, L., and Gennaretti, M., "Boundary Integral Equation Methods for Aerodynamics," *Computational Nonlinear Mechanics in Aerospace Engineering*, edited by S. N. Atluri, Vol. 146, Progress in Astronautics and Aeronautics, AIAA, New York, 1992, pp. 279–320.

[20] Morino, L., and Bharadvaj, B. K., "A Unified Approach for the Potential and Viscous Free-Wake Analysis of Helicopter Rotors," *Vertica*, Vol. 12, No. 1/2, 1988, pp. 147–154.

[21] Leishman, J. G., *Principles of Helicopter Aerodynamics*, Cambridge Univ. Press, Cambridge, England, U.K., 2000.

[22] Hodges, D. H., and Dowell, E. H., "Nonlinear Equation for the Elastic Bending and Torsion of Twisted nonuniform Rotor Blades," NASA TN D-7818, Dec. 1974.

[23] Hodges, D. H., and Ormiston, R. A., "Stability of Elastic Bending and Torsion of Uniform Cantilever Rotor Blades in Hover with Variable Structural Coupling," NASA TN D-8192, April 1976.

[24] Favier, D., Ettaouil, A., and Maresca, C., "Numerical and Experimental Investigation of Isolated Propeller Wakes in Axial Flight," *Journal of Aircraft*, Vol. 26, No. 9, 1989, pp. 837–846. doi:10.2514/3.45849

[25] Theodorsen, T., "General Theory of Aerodynamic Instability and the Mechanism of Flutter," NACA Rept. 496, 1935.

[26] Greenberg, J. M., "Airfoil in Sinusoidal Motion in a Pulsating Stream," NACA TN-1326, June 1947.